Polyhedron 177 (2020) 114302

Contents lists available at ScienceDirect

Polyhedron

journal homepage: www.elsevier.com/locate/poly

Sonochemical synthesis of $ErVO_4/MnWO_4$ heterostructures: Application as a novel nanostructured surface for electrochemical determination of tyrosine in biological samples

Asma Khoobi [a], Faezeh Shahdost-fard [b,c], Mohsen Arbabi [d,e], Maryam Akbari [f], Hamed Mirzaei [e,g], Majid Nejati [e,h], Majid Lotfinia [e,i], Ali Sobhani-Nasab [e,j,*], Hamid Reza Banafshe [i,k,*]

[a] Department of Analytical Chemistry, Faculty of Chemistry, University of Kashan, Kashan, P.O. Box. 87317-51167, Islamic Republic of Iran
[b] Department of Chemistry, Ilam University, Ilam, Iran
[c] Faculty of Medicine, Ilam University of Medical Sciences, Ilam 69391-77143, Iran
[d] Department of Medical Parasitology and Mycology, School of Medicine, Kashan University of Medical Sciences, Kashan, Iran
[e] Core Research Lab, Kashan University of Medical Sciences, Kashan, Iran
[f] Department of Surgery, School of Medicine, Kashan University of Medical Sciences, Kashan, Iran
[g] Research Center for Biochemistry and Nutrition in Metabolic Diseases, Institute for Basic Sciences, Kashan University of Medical Sciences, Kashan, Iran
[h] Anatomical Sciences Research Center, Kashan University of Medical Sciences, Kashan, Iran
[i] Physiology Research Center, Institute for Basic Sciences, Kashan University of Medical Sciences, Kashan, Iran
[j] Social Determinants of Health (SDH) Research Center, Kashan University of Medical Sciences, Kashan, Iran
[k] Department of Pharmacology, School of Medicine, Kashan University of Medical Sciences, Kashan, Iran

ARTICLE INFO

Article history:
Received 25 July 2019
Accepted 18 November 2019
Available online 12 December 2019

Keywords:
$ErVO_4/MnWO_4$
Heterostructures
Sonochemical method
Tyrosine
Biological sensor

ABSTRACT

Present strategy introduces a novel method established for the synthesis of spherical shape $ErVO_4/MnWO_4$ heterostructures by a sonochemical method. This heterostructures with optima morphology can be synthesized by changing power and time ultrasound irradiation without any capping agent. BET analysis revealed that $ErVO_4/MnWO_4$ prepared in the presence of ultrasonic procedure has 75 times specific surface area as much as that of those was produced in the absence of ultrasonic rays. A variety of analyses (i.e., BET, XRD, TEM, EDS, FT-IR, and SEM) were applied for characterization of the $ErVO_4/MnWO_4$. Next, a selective and sensitive nanostructured sensor based on $ErVO_4/MnWO_4$ nanocomposite modified carbon paste electrode ($ErVO_4/MnWO_4$/CPE) was constructed for electrochemical detection of tyrosine (Tyr). The electrochemical characterizations were performed using cyclic voltammetry (CV), electrochemical impedance spectroscopy (EIS) and differential pulse voltammetry (DPV). Compared with the unmodified CPE, the oxidation peak current was significantly enhanced for Tyr. The impact of effective parameters on voltammetric response of Tyr was analyzed with design of experiments (DOE) and response surface methodology (RSM). Under the optimized conditions, the oxidation peak current of Tyr was linear over a range of 0.08–400.0 μM with a detection limit of 7.7 nM. Finally, the usage of the proposed method was confirmed by the recovery tests of Tyr in biological samples.

1. Introduction

Current medical advances have focused on the hygienic, personal and community health issues to find novel and effective biomolecules. In this regards, any development in medical and hygienic fields has resulted in a more requirements to establish better accurate measurement methods. Proteins are one of very important components of all cells which have crucial roles in wide ranges of biological processes, and are composed of different amino acids. Of various amino acids, Tyrosine (Tyr) is a main amino acid which has major roles in protein structures. This amino acid is used as protein-based supplements for treatment of various types of genetic disorder such as phenylketonuria (PKU). Tyr is also being utilized to improve learning, memory, and consciousness in stressful conditions. The producer of important chemical materials in brain can help neurons to communicate and possibly they are able to adjust our tempers [1,2].

* Corresponding authors at: Social Determinants of Health (SDH) Research Center, Kashan University of Medical Sciences, Kashan, Iran (A. Sobhani-Nasab). Physiology Research Center, Kashan University of Medical Sciences, Kashan, Iran (H. R. Banafshe).

E-mail addresses: Ali.sobhaninasab@gmail.com (A. Sobhani-Nasab), Banafshe57@hotmail.com (H.R. Banafshe).

https://doi.org/10.1016/j.poly.2019.114302
0277-5387/

It is described that the abnormal amount of Tyr is directly associated to several human diseases. High level of Tyr can cause dementia or Parkinson's disease while lack of the compound may lead to hypochondrium, depression, alkaptonuria and albinism [3]. Therefore, it is very important to develop an accurate, rapid, simple and inexpensive method for detection of low concentrations of Tyr. Several methods have been employed for measurement of Tyr including spectroflurometric [4], spectrophotmetric [5], electrochemistry [6] and high performance liquid chromatography (HPLC) methods [7]. Response surface methodology (RSM) and designs of experiments (DOE) are strategies to collect empirical knowledge based on the study of experimental data. Furthermore, the experimental parameters of differential pulse voltammetry (DPV) have an important influence on the peak currents of analytes at the surface of nanostructured modified electrodes. Also, an effective experimental design method was introduced for process of analysis and modeling of central composite design (CCD) [8]. Metal tungstate and lanthanide vanadate have been prepared by different methods such as hydrothermal, solid-state reaction, precipitation, sol–gel, and microwave methods [9–14]. Given that utilization of sonochemical methods are associated to some advantages, nanomaterials which have been synthesized by these strategies have a faster reaction times, higher surface area, uniform size distribution, and improved phase purity [15]. $ErVO_4$/$MnWO_4$ heterostructures was successfully prepared for the first time by simple and novel ultrasonication method without the aid of capping agent. The impact of the kind of ultrasonic time and power on the quality crystals and morphology of this heterostructures has been evaluated for optimization of the production condition. We assessed $ErVO_4$/$MnWO_4$ heterostructures by Brunauer–Emmett–Teller (BET), X-ray diffraction (XRD), transmission electron microscopy (TEM), energy-dispersive X-ray spectroscopy (EDS) Fourier transform infrared spectroscopy (FT-IR), and scanning electron microscopy (SEM) techniques.

In this work, a sonochemical method was applied for synthesis of our final products. Then, a sensitive $ErVO_4$/$MnWO_4$ heterostructures modified carbon paste electrode ($ErVO_4$/$MnWO_4$/CPE) was designed for determination of Tyr amino acid. Also, the influence of experimental factors on the DPV peak current of Tyr was evaluated based on multi-factor interaction effects. Accordingly, the determination of Tyr was accomplished based on $ErVO_4$/$MnWO_4$/CPE using DPV, under the optimized conditions. Additionally, the feasibility and practicality of the nanostructured sensor were confirmed by the detection of Tyr in biological samples. To our best of knowledge, no method using $ErVO_4$/$MnWO_4$ heterostructures and multivariate optimization has been reported for determination of Tyr.

2. Materials and methods

2.1. Materials

Ammonium vanadate, Erbium (III) nitrate, Sodium tungstate, Manganese nitrate, Tyr, carbon graphite powder, paraffin oil, and other chemicals were purchased from Merck. Stock solutions of 0.2 M H_3BO_3, H_3PO_4, CH_3COOH, and a saturated solution of NaOH were applied for preparation of 0.2 M Britton-Robinson (B-R) buffer. All solutions were prepared using analytical grade chemicals and deionized water.

2.2. Structural characteristics of $ErVO_4$/$MnWO_4$ heterostructures

The morphology and size in the preparation of $ErVO_4$/$MnWO_4$ were performed using the field emission gun-transmission electron microscope (FEF-TEM200 kV, Jeol JEM-2100F, Tokyo, Japan). For the elemental analysis of the heterostructures, Energy- dispersive X-ray spectroscopy (EDX) was performed during SEM imaging. The structural characterization of the heterostructures was analyzed by Smart lab Rigaku Diffractometer (XRD) which was functioning at 20 kV in continuous scanning step-scans mode. The XRD was recorded as a function of 2θ angle, ranging from 10° to 80°, with a step size of 0.01° and scanning speed of 0.1 s/step using a monochromatic X-ray beam by applying a diffractometer of Philips Company with X'Pert promonochromatized Cu K_α radiation (k = 1.54 Å). We plotted the obtained XRD data with no software processing except for background subtraction. The FTIR study of the compound was done using a Nicolet Magna- 550 spectrometer

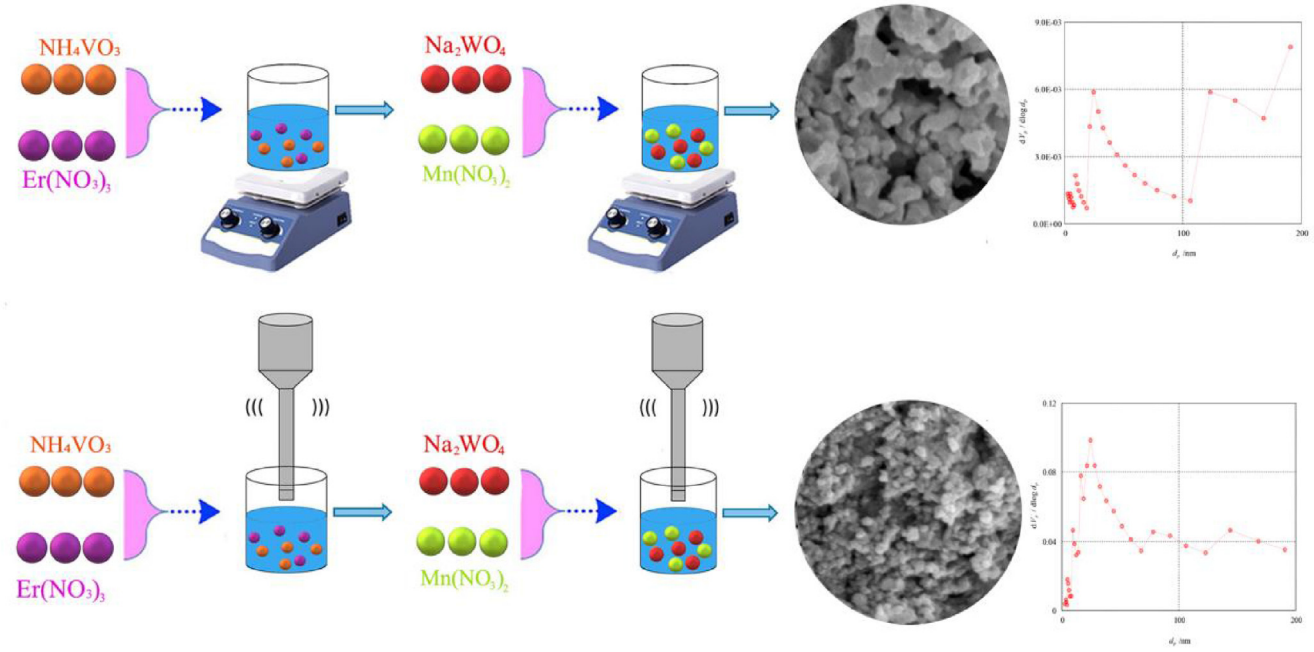

Scheme 1.

Table 1
The preparation conditions of the $ErVO_4$ nanostructures and $ErVO_4/MnWO_4$ heterostructure.

Sample No	Power	Sonication time (min)	Calcined temperature °C	Crystal size	Product	Figure of SEM images
1	60	5	500	22	$ErVO_4$	–
2	60	5	–	–	$ErVO_4/MnWO_4$	–
3	60	5	500	24	$ErVO_4/MnWO_4$	Fig. 3a
4	120	5	500	23	$ErVO_4/MnWO_4$	Fig. 3b
5	180	5	500	21	$ErVO_4/MnWO_4$	Fig. 3c
6	180	10	500	18.9	$ErVO_4/MnWO_4$	Fig. 4a
7	180	15	500	18.2	$ErVO_4/MnWO_4$	Fig. 4b
8	180	20	500	17	$ErVO_4/MnWO_4$	Fig. 7b
9	–	–	500	29	$ErVO_4/MnWO_4$	Fig. 5a

Table 2
The adsorption/desorption parameter of the $ErVO_4/MnWO_4$ heterostructure prepared with and without ultrasonic wave.

Product	Power	Total pore volume	Mean pore diameter	Specific surface areas
$ErVO_4/MnWO_4$	–	0.00505	190.55	1.4109
$ErVO_4/MnWO_4$	180	0.3733	67.63	106.50

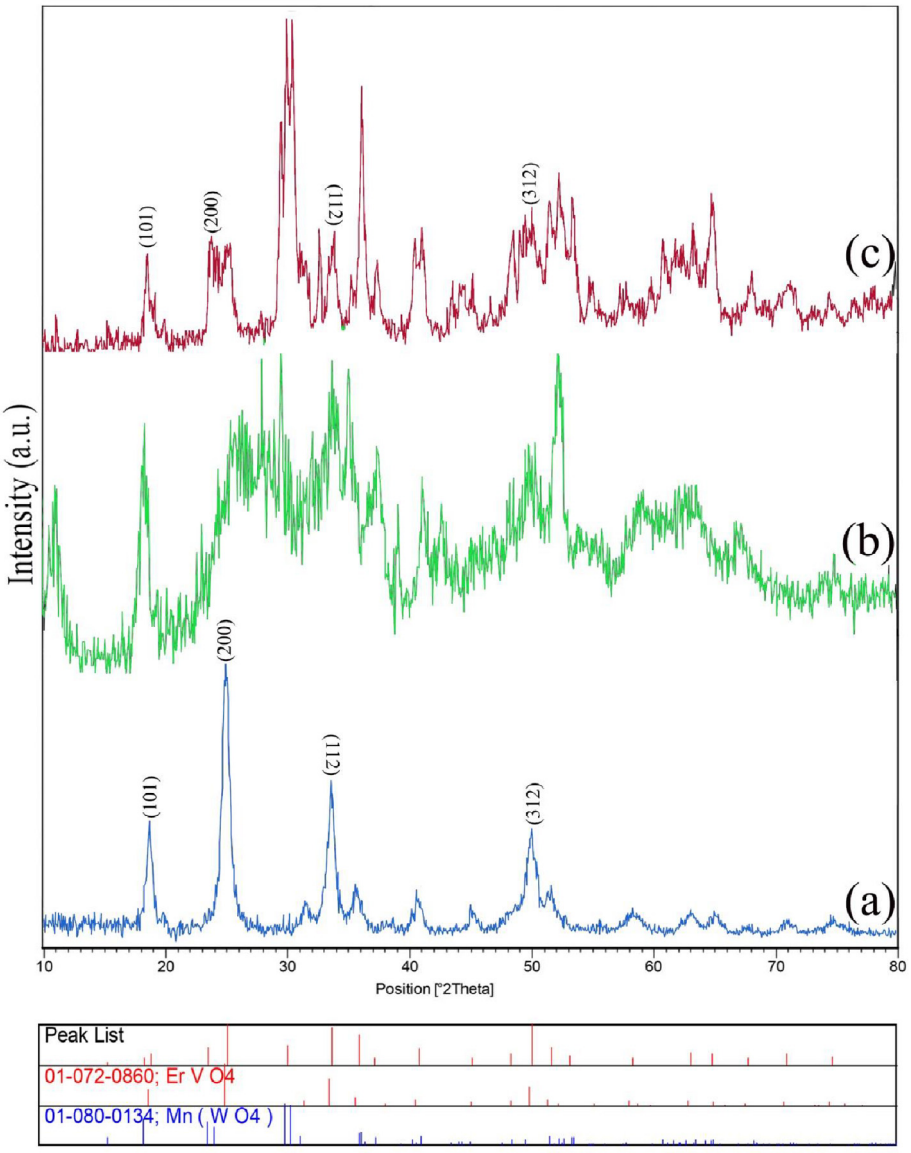

Fig. 1. XRD pattern of nanostructure obtained under ultrasonic wave for 5 min with power 60 W (a) $ErVO_4$ at 500 °C, (b) $ErVO_4/MnWO_4$ at 25 °C and (c) $ErVO_4/MnWO_4$ at 500 °C.

and KBr pellets with all three batches as a function of percentage transmittance by a 3000 hyperion microscope with vertex 80 FTIR system which had a spectral resolution of 0.2 cm^{-1} and scan speed of 65 spectra/s at 16 cm^{-1}. Thermal degradation or thermal stability study of heterostructures were done by employing a thermal gravimetric analysis instrument (Shimadzu TGA-50H) with a flow rate of 30.0 mL min °C and a heating rate of 22 °C min with heterostructures performed on thermo gravimetric analyzer (TGA) (Perkin Elmer USA, Diamond TG/DTA). The surface area in characterization of the heterostructures was performed on SMART SORB 92/93, Brunauer-Emmett-Teller (BET) surface area analyzer. The N_2 adsorption/desorption analysis was performed to calculate the surface area.

2.3. Synthesis of $ErVO_4/MnWO_4$ heterostructures

1 mmol of erbium nitrate in 30 ML of double distilled water was dissolved in room temperature. Furthermore, 1 mmol of ammonium vanadate was dissolved in 30 ML of distilled water in 70 °C for 30 min under constant magnetic stirring. Then we added urbium nitrate solution into ammonium vanadate with ultrasonic waves in room temperature. On the other hand, we separately dissolved 1 mmol of Mn nitrate and Na tungstate in double distilled water with pH = 5 in room temperature. Firstly, the sodium tungstae solution was added into erbium vanadate solution. Afterwards, the manganese tungstae was added drop wise into the solution including nanostructure erbium vanadate and sodium tungstate under ultrasonic rays in normal temperature. The yellowish brown precipitation presents the fabrication of $ErVO_4/MnWO_4$ heterostructures. Finally, the compound was calcined for 1 h in 500 °C. Then, we investigated optimization of power and time in ultrasonic waves to reach optimum morphology. Also, all sages in fabrication of heterostructures were done without the presence of ultrasonic waves Scheme 1. The different conditions for preparation of heterostructures have come to show in Table1.

2.4. Electrochemical studies

Electrochemical impedance spectroscopy (EIS) analysis was performed using an Autolab potentiostat-galvanostat PGSTAT 35 (Eco Chemie Utrecht, Netherlands), equipped with NOVA 1.6 software. Other electrochemical studies were carried out by a Sama 500 potentiostat (Iran). A conventional three electrode systems containing $ErVO_4/MnWO_4$/CPE, an Pt wire (Metrohm, Switzerland) and Ag/AgCl/KCl (3.0 M) (Metrohm, Switzerland) were applied as working, counter and reference electrodes, respectively.

The CPE was constructed by mixing of 0.5 g graphite powder with 0.18 g of paraffin oil in pestle mortar. For preparation of $ErVO_4/MnWO_4$/CPE, optimum amount of $ErVO_4/MnWO_4$ heterostructures was added to ethanol and sonicated for 30 min

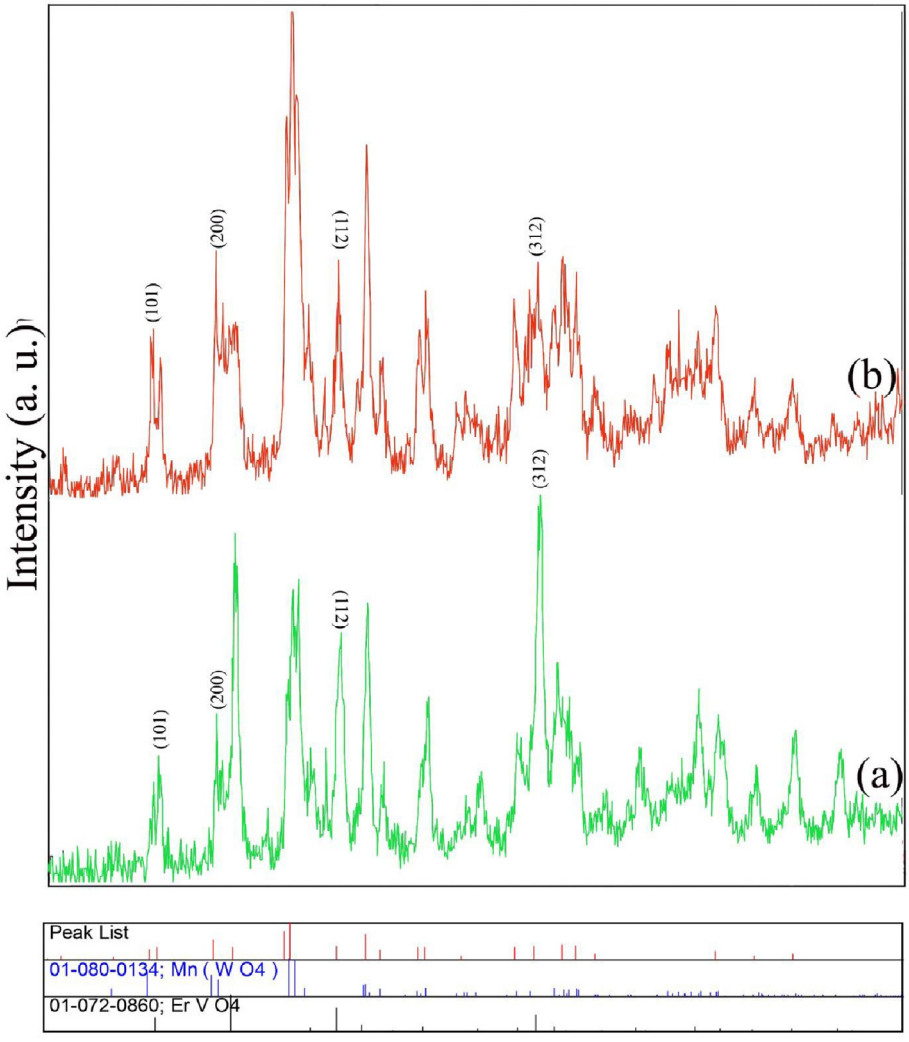

Fig. 2. XRD pattern of $ErVO_4/MnWO_4$ heterostructure obtained under ultrasonic wave for 5 min with power (a) 120 W and (b) 180 W at 500 °C.

to create a homogenous suspension. The optimum amount was calculated based on multivariate optimization method. Next, this suspension was mixed with 0.5 g of graphite powder and ethanol was evaporated. Then, 0.18 g of paraffin oil was added and mixed to achieve a uniform paste. Finally, the paste was packed into a cavity of the electrode body and the surface of the electrode polished by a weighing paper. Also, electrical connection to the paste was established by a copper wire.

2.5. Optimization strategy and data analysis

The effects of process parameters, containing pH (X_1), amount of $ErVO_4/MnWO_4$ heterostructures (X_2), step potential (X_3) and pulse height (X_4) were assessed using a rotatable central composite design (RCCD) in the form of (RSM). Five levels for each factor were considered to carry out the experiments. Data analysis was studied using the MINITAB®Release 16, developed by Minitab Inc. (USA)

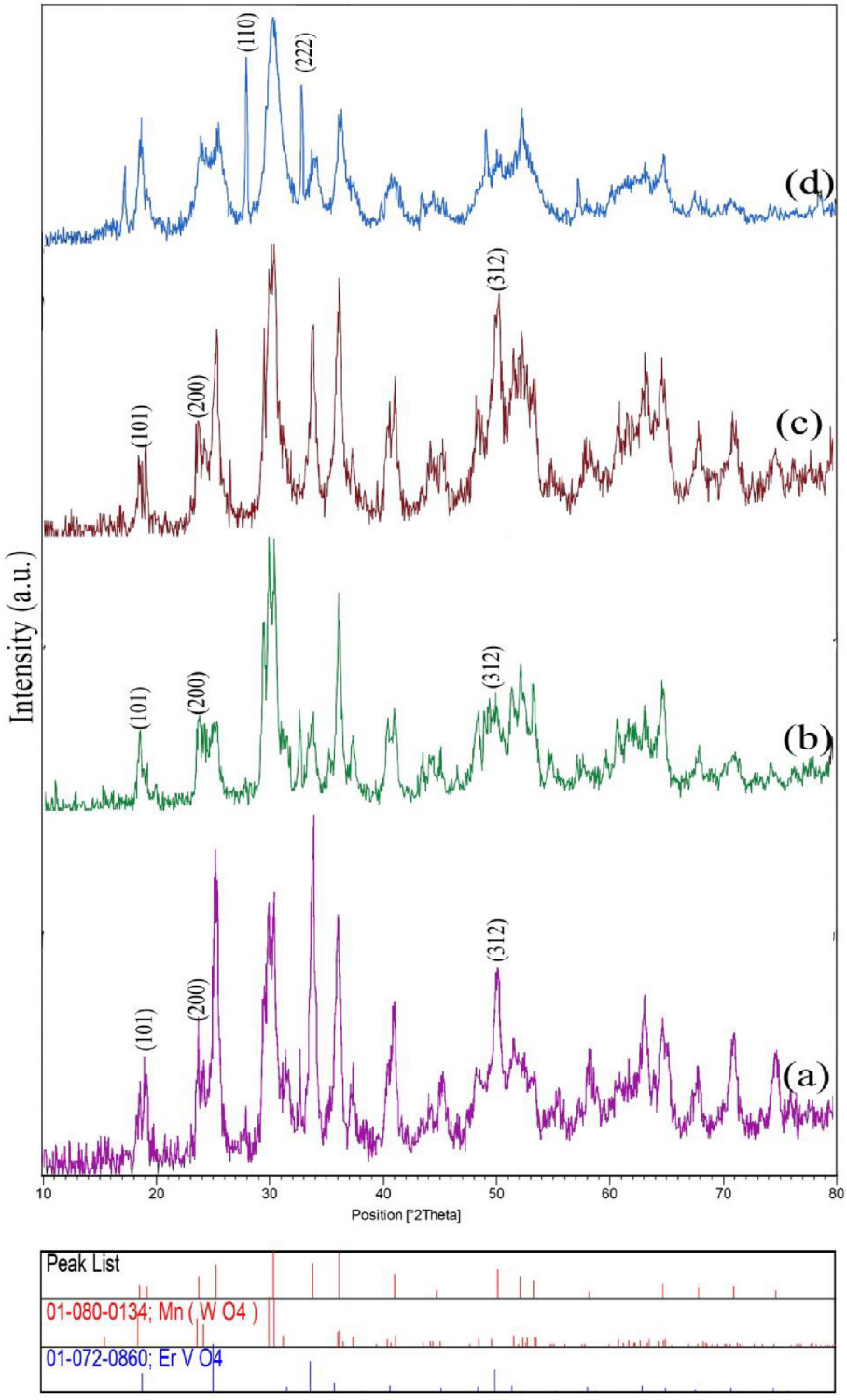

Fig. 3. XRD pattern of $ErVO_4/MnWO_4$ heterostructure obtained under ultrasonic wave with power 180 W for (a) 10 min (b) 15 min, (c) 20 min and (d) without ultrasonic wave at 500 °C.

software. Four independent variables, pH (5.00–9.00, X_1), $ErVO_4$/$MnWO_4$ heterostructures amount (1.00–5.00 mg, X_2), step potential (0.001–0.009 V, X_3) and pulse height (0.02–0.06 V, X_4) were evaluated at 5 levels with 3 replicate at the center point and α calculated ±2 [28]. Thus, we needed 4 parameters and 27 tests to run for optimizing of factors. The coded and actual level values of each parameter are presented in Table 2.

3. Results and discussion

3.1. Characterization

X-ray analysis is being extensively applied in research for obtaining the crystal structure and purity of nanostructures [16–21]. The XRD pattern of $ErVO_4$ nanostructures with a power of 60 W is displayed in Fig. 1a. The spectrum of bare $ErVO_4$ nanostructures shows a series of diffraction peaks at the position of 18.86°, 25.07°, 33.67° and 49.92° with lines (1 0 1), (2 0 0), (1 1 2) and (3 1 2), respectively which is in good agreement with the tetragonal phase with space group of *I*41/*amd* (JCPDS 01–072-0860) and calculated cell parameters of a = b = 7.0975 Å and c = 6.2723 Å [22].

$ErVO_4$/$MnWO_4$ was prepared in room temperature and calcined in 500 °C to investigative the effect of temperature on the crystal structure. Besides, the XRD pattern of $ErVO_4$/$MnWO_4$ prepared in room temperature with low crystallinity has been displayed in Fig. 1b. The XRD pattern of $ErVO_4$/$MnWO_4$ heterostructure prepared with power of 60 W and 5 min in 500 °C has been displayed in Fig. 1c. $ErVO_4$/$MnWO_4$ heterostructure is pure and composed of $ErVO_4$ (JCPDS 01–072-0860 and space group of *I*41/*amd*) and $MnWO_4$ (JCPDS 01–080-0134 and space group of *P*2/*c*) shows a series of diffraction peaks at the position of 18.48°, 29.98°, 30.46° and 51.61° with lines (1 0 0), (1 1 1), (1 1 1) and (1 3 0), respectively which is in good agreement with the tetragonal phase and calculated cell parameters of a = 4.7980b = 5.7106 Å and c = 4.9738 Å [30]. From the Fig. 1(c), one can confirm the presence of XRD peaks of $ErVO_4$/$MnWO_4$ heterostructure. The average crystallite diameter was calculated using Debye-Scherrer [23] formula, and it found to be 35 nm.

To investigate effects of ultrasonic irradiation on structure of crystal in heterostructure, we used such waves with the power of 120 W and 180 W (Fig. 2a, b). Our calculation showed that heterostructure prepared with the power of 120 and 180 W has the size of 27 and 23 nm, respectively. Therefore, increasing of power can result in decrease in the size of $ErVO_4$/$MnWO_4$ heterostructure. Then, we verified the influence of time on the structure and size of crystals. To do so, we prepared $ErVO_4$/$MnWO_4$ heterostructure with the power of 180 W and time 10, 15, 20 min under ultrasonic waves. According to the Fig. 3a–c with increasing time, the size of crystals reduced from 23 to 16 nm. Hence, simply, one can conclude that the trend of reduction in the size of crystals matches the SEM images. The prepared $ErVO_4$/$MnWO_4$ without ultrasonic irradiation as shown in Fig. 3d. according to this figure, ultrasonic waves not only can reduce the size of crystals but also can produce pure $ErVO_4$/$MnWO_4$ heterostructures.

We used the FTIR analysis in the range of 400–4000 cm^{-1} to evaluate the composition and quality of the $ErVO_4$ and $ErVO_4$/$MnWO_4$ heterostructures as shown in Fig. 4(a and b). In Fig. 4(a) the peak at 3441.96 cm^{-1}, which corresponds to O—H stretching of water molecules is presented in $ErVO_4$ [24]. A week band was observed at 1632.26 cm^{-1} corresponding to Bending band of intercalated O—H in water. The observed peak at 817.77 and 451.81 cm^{-1}, which corresponds to O-V-O and Er-O stretching vibrations exist in $ErVO_4$ [25]. The FT-IR spectrum of the compound has been shown in Fig. 4b. which clearly exhibits a red shift in compare with $ErVO_4$ nanostructure. The FT-IR spectrum shows two peaks at 3438.55 and 1635.24 cm^{-1} which related to bending and stretching vibrations available in water. The observed peak at 828.28 and 488.93 cm^{-1}, which is related to the V-O and Er-O stretching vibrations exist in $ErVO_4$. Furthermore, two strong peaks associate with stretching vibrations of W-O (935.94 cm^{-1}) and Mn-O (595.32 cm^{-1}) confirm pure $ErVO_4$/$MnWO_4$ heterostructures [13]. Based on the Fig. 5, sample No. 4 consists of Mn, W, Er, V, and O elements. Furthermore, neither N nor C signals were observed in the EDS spectrum suggesting the product is pure and has no surfactant or impurity.

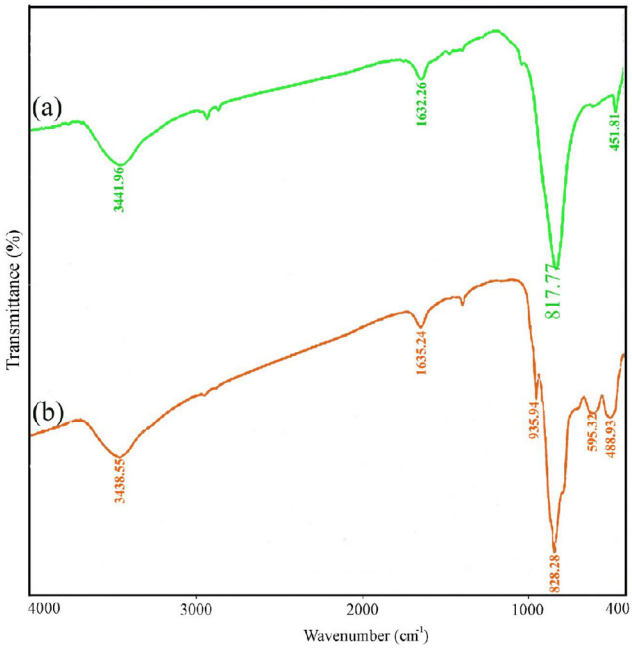

Fig. 4. FT-IR spectra of (a) $ErVO_4$ and (b) $ErVO_4$/$MnWO_4$ heterostructure.

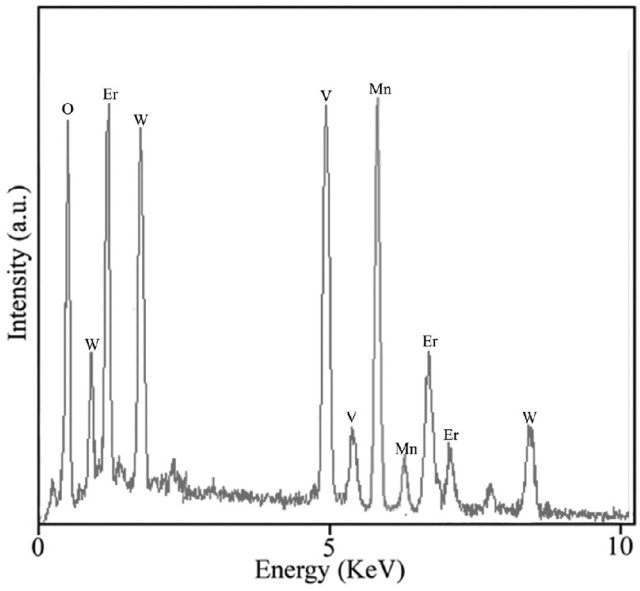

Fig. 5. EDS pattern of $ErVO_4$/$MnWO_4$ heterostructure under ultrasonic wave for 20 min with power 180 W (Sample No. 8).

3.2. Sonication mechanism

Of all procedures for preparation of nanoscaled particles high intensity ultrasound is considered to be the most controllable and uncomplicated method. Currently, subjecting materials to ultrasonic rays have received much focus [26–31]. All together, by above mentioned method, water can turn into H· and OH· radicals. Current paper contains the proposed procedure stating reduction of VO^{3-} in presence of H_2O_2 to generate VO_4^{3-}. In these consecutive reactions, these two · radicals are successful to make H_2O_2 as following [32]:

$$H_2O)))) \rightarrow H^{\hat{A}\cdot} + OH^{\hat{A}\cdot} \quad (3)$$

$$OH^{\hat{A}\cdot} + OH^{\hat{A}\cdot} \rightarrow H_2O_2 \quad (5)$$

$$H^{\hat{A}\cdot} + H^{\hat{A}\cdot} \rightarrow H_2 \quad (4)$$

$$H^{\hat{A}\cdot} + O_2 \rightarrow HO_2^{\hat{A}\cdot} \quad (6)$$

$$H^{\hat{A}\cdot} + HO_2^{\hat{A}\cdot} \rightarrow H_2O_2 \quad 7)$$

$$HO_2^{\hat{A}\cdot} + HO_2^{\hat{A}\cdot} \rightarrow H_2O_2 + O_2 \quad (8)$$

In which the symbol)))) is related to the exerting ultrasound rays. Obviously, for making $HO_2^{\cdot}$ radicals both OH· and H· radicals should be mixed with each other. Moreover, the combination of two $HO_2^{\cdot}$ radicals can lead to production of H_2O_2. Other reaction equation refers to combination of two OH· radical with 10 making hydrogen peroxide. Nevertheless, these radicals can influence the process of making of products [33]. The first precursors can disperse in water to form ions. In this attempt, these kinds of precursors are not volatile, and are ionic. Hence one can conclude the occurrence of reaction between cavitation bubbles and bulk of solution. Since ionic precursors have low vapor pressure, they are not able to penetrate in the inner region of the cavitation in liquid-free zone. Provided that such ions are in suitable condition, they are able to form nanosized $ErVO_4$ subordinate to sonication method. Finally, Er^{3+} reacts with $VO4^{3-}$ ions leading to $ErVO_4$ nanoparticles [34]. Based on the reactions presented in the below one can possibly suggest that hydrogen peroxide and product can have direct reaction with each other. Also, we can deduce that the value of hydrogen peroxide is positively connected with $ErVO_4$ nanostructures. It means the rate of nucleation can enhance with increase in the formation of H_2O_2. Besides, fast nucleation can lead to a significant amount of nuclei and as a result the crystal growth step could be shortened. This, in turn, ends in production of very tiny particles. This study shows that ultrasonic method can improve fast production of hydrogen peroxide, and as a result, quick nucleation can lead to production of very small size with short time [35].

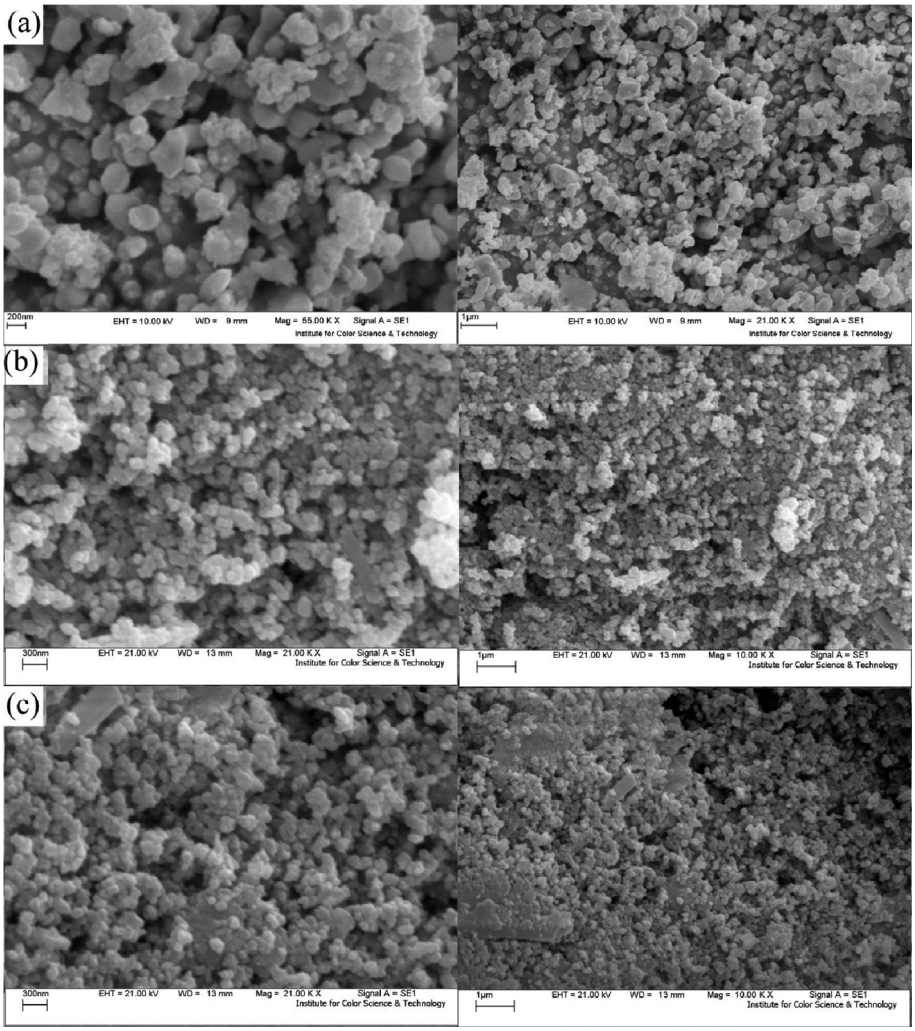

Fig. 6. SEM images of $ErVO_4/MnWO_4$ heterostructure obtained under ultrasonic wave for 5 min with power (a) 60 W (b) 120 W and (c) 180 W.

$$Er(NO_3)_3.6H_2O + H_2O \rightarrow Er^{3+} + 3NO_3^- + 7H_2O \quad (11)$$

$$NH_4VO_3 + H_2O \rightarrow NH_4^+ + VO_4^- + H^+ + OH^- \quad (9)$$

$$VO_3^- + H_2O_2)))) \rightarrow 3VO_4^{3-} + H_2O \quad (10)$$

$$Er^{3+} + VO_4^{3-} \rightarrow ErVO_4 \quad (12)$$

$$Mn(NO_3)_2.6H_2O + H_2O \rightarrow Mn^{2+} + 2NO_3^- + 7H_2O \quad (15)$$

$$Na_2WO_4 + H_2O \rightarrow 2Na^+ + WO_4^{2+} + H^+ + OH^- \quad (13)$$

$$Mn^{2+} + WO_4^{2+} \rightarrow MnWO_4 \quad (16)$$

$$NH_4{}^+ + NO_3^- \rightarrow NH_4NO_3 \quad (17)$$

$$Er(NO_3)_3.6H_2O + 3NH_4VO_3 + Mn(NO_3)_2.6H_2O + 2Na_2WO_4 + \rightarrow NH_4NO_3 + NaNO_3 + ErVO_4/MnWO_4 + H_2O \quad (18)$$

In this procedure cavitation is occurred and as a result, high local temperature and pressure are made in reaction medium. This procedure includes the formation, gradual growth, and eventually, explosion of a series of bulbs [36]. The energies produced for such

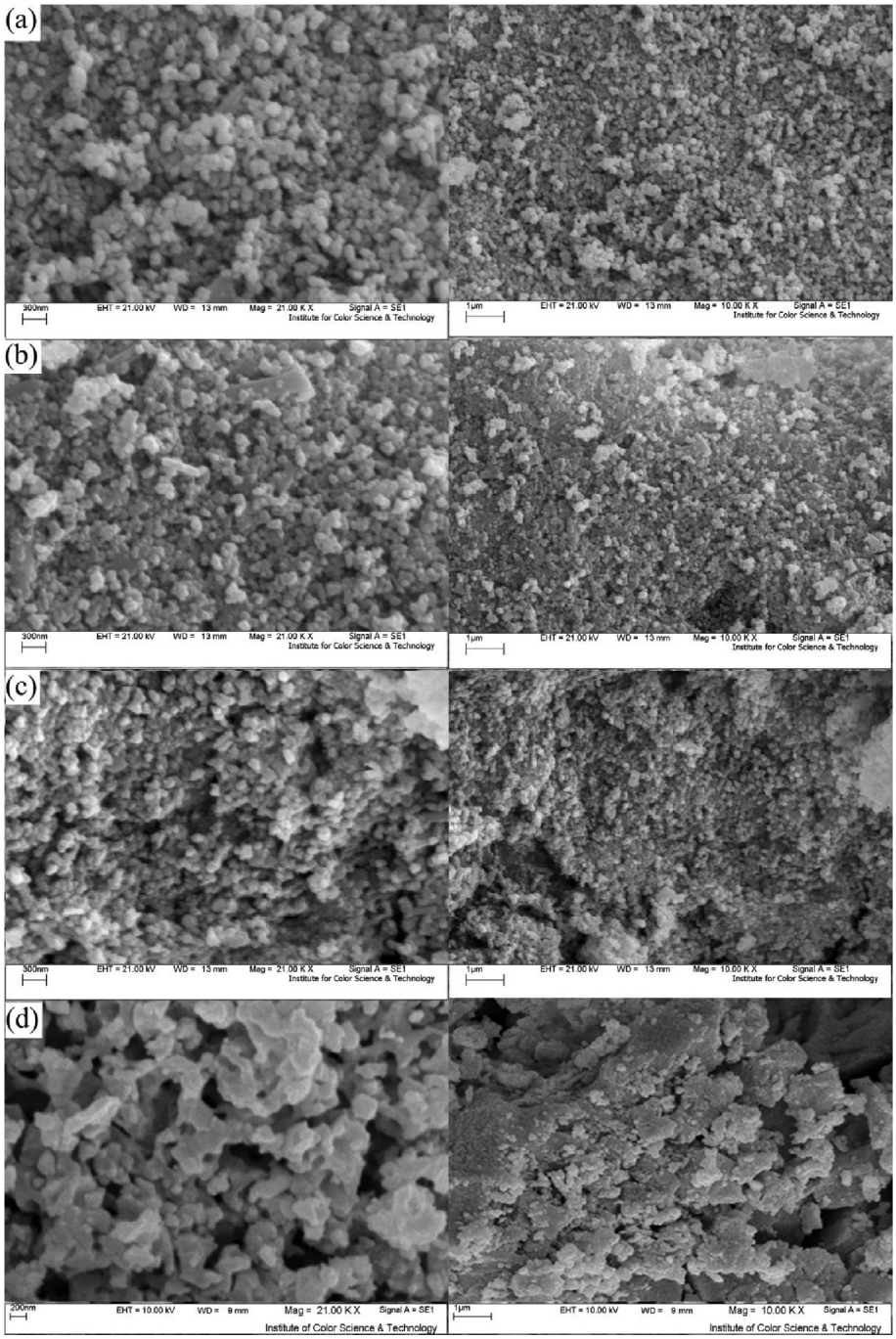

Fig. 7. SEM images of $ErVO_4/MnWO_4$ heterostructure obtained under ultrasonic wave with 180 W for 10 min 15 min 20 min and without ultrasonic wave.

wave can break covalent bond. Also it could be used for homogenization and performing of some chemical reactions such as the synthesis of nanoparticles, organic materials, and so forth [36–38]. Consequently, increasing power of waves from 60 to 180 W can result in enhancement in shock waves and the reduction in the size of $ErVO_4/MnWO_4$ heterostructures (Fig. 6a–c). For investigation of further parameters on morphology of $ErVO_4/MnWO_4$ heterostructures, the time was used, and it was prepared in the different times 10, 20, and 30 (Fig. 7a–c). Therefore, increase in the time of ultrasonic rays can lead to increase in implosive collapse, and the size of heterostructures can reduce. Hence, the preparation of heterostructures in the presence of ultrasonic waves with the power of 180 W in half an hour can produce heterostructures with the size of 40–70 nm. Furthermore, they have spherical morphology and equal size of distribution. In Fig. 7d, we have shown the fabrication of $ErVO_4/MnWO_4$ heterostructures in the absence of ultrasonic waves. So, making use of ultrasonic waves could be considered as a method to any reduction in both size and agglomeration of the heterostructures. The TEM different magnification images are used to confirm the morphology of $ErVO_4/MnWO_4$ heterostructures as shown in Fig. 8, showing it has spherical shape structure with mean diameter range of 30–60 nm.

3.3. BET analysis

For the investigation of specific surface area and pore volume we used BET analysis. We have shown the adsorption/desorption isotherm and the plot of JH in the Fig. 9a and b (in the absence of ultrasonic waves) and Fig. 9 c and d (in the presence of ultrasonic waves with the power of 180 W in 20 min), respectively. According to IUPAC classification, adsorption isotherm of $ErVO_4/MnWO_4$ heterostructures belongs to type II isotherm. An explanation for the size of disordered pores for $ErVO_4/MnWO_4$ heterostructures prepared in the absence of ultrasonic waves has shown in Fig. 9 a. The mean pore, specific surface areas and total pore volume and diameter for this sample were calculated to be 190.55 nm, 1.4109 m^2/g and 0.00505 cm^3/g, respectively. The distribution of the size of pores in heterostructures prepared in the presence of ultrasonic waves has displayed in Fig. 9b. According to the figure, $ErVO_4/MnWO_4$ heterostructures have been distributed well, and the maximum size of pores is 65 nm. The mean pore, specific surface areas and total pore volume and diameter for this sample was found to be 67.63 nm, 106.50 m^2/g and 0.3733 cm^3/g, respectively (Table 2).

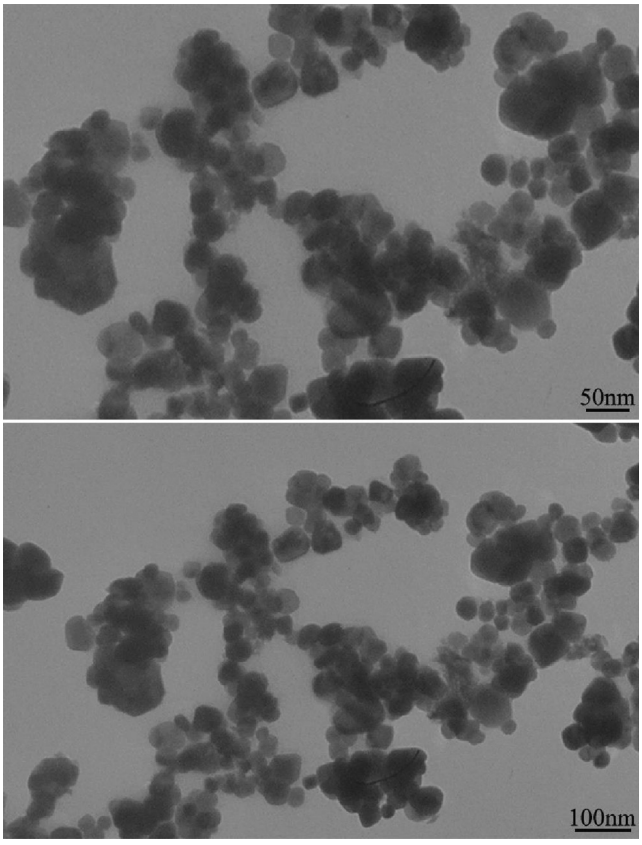

Fig. 8. TEM image of $ErVO_4/MnWO_4$ heterostructure obtained under ultrasonic wave with power 180 W for 20 min.

3.4. TGA analysis

The thermal Gravimetric analysis for $ErVO_4$ nanoparticles and $ErVO_4/MnWO_4$ heterostructures has been shown in Fig. 10. As one can see, the weight of sample changed within 2 steps. First one includes from 27 °C to 225 °C, which is related to the evaporation of water molecules, and is physical absorbent. In 225 °C water molecules completely evaporated from the surface of sample. The second step involves in 225–425 °C. In this stage the chemical absorbent water molecules evaporated and additional compounds existed in the sample such as nitrates vaporized as well. Therefore, our findings showed that nanostructures have high stability and combining with $MnWO_4$ in $ErVO_4$ can lead to increase in stability of heterostructures [39].

3.5. Analytical applications

3.5.1. Catalytic effect of $ErVO_4/MnWO_4$ heterostructures

Electrocatalytic activity of $ErVO_4/MnWO_4$ heterostructures was examined using cyclic voltammetry (CV) technique. The cyclic voltammetric tests were performed in the present of 5.0 mM redox probe $K_3Fe(CN)_6 + K_4Fe(CN)_6$) B-R solution (0.2 M, pH 7.0). Fig. 11 shows the cyclic voltammograms of the CPE and $ErVO_4/MnWO_4$/CPE. It is clear that the $ErVO_4/MnWO_4$/CPE displays well defined redox peaks with enhanced current response and reduction in ΔEp than the bare CPE. On the other hand, the peak potential difference ΔE_p decreases in the order CPE > $ErVO_4/MnWO_4$/CPE, which corresponds to the increasing rate constant of electron transfer in the opposite order. The phenomena suggest that $ErVO_4/MnWO_4$/CPE exhibits faster electron transfer kinetics and possess larger electroactive surface area compared to CPE. It approves the strong electrocatalytic ability of the $ErVO_4/MnWO_4$ heterostructures that shows the nanostructures can be acts as a potential surface for sensitive determination of Tyr. The electrocatalytic mechanism for redox probe $K_3Fe(CN)_6 + K_4Fe(CN)_6$) can be described as follow: as the potential is scanned positively (forward scan, here) and is sufficiently positive to oxidize $Fe(CN)_6^{-4}$, the anodic current is due to the electrode process ($Fe(CN)_6^{4-} \rightarrow Fe(CN)_6^{3-} + e$). Therefore, the electrode acts as an oxidant and the oxidation current increases to a peak. The concentration of $Fe(CN)_6^{-4}$ at the electrode surface depletes and the current then decays. As the scan direction is switched to negative, for the reverse scan the potential is still sufficiently positive to oxidize $Fe(CN)_6^{-4}$, so anodic current continues even though the potential is now scanning in the negative direction. When the electrode becomes a sufficiently strong reductant, $Fe(CN)_6^{-3}$, which has been forming adjacent to the electrode surface, will be reduced by the electrode process ($Fe(CN)_6^{3-} + e \rightarrow Fe(CN)_6^{4-}$), resulting in a cathodic current which peaks and then decays as $Fe(CN)_6^{3-}$ in the solution adjacent to the electrode is consumed. In the forward scan $Fe(CN)_6^{-3}$ is electrochemically generated from $Fe(CN)_6^{-4}$ (anodic process) and in the reverse scan this $Fe(CN)_6^{-3}$ is reduced back to $Fe(CN)_6^{-4}$ (cathodic process).

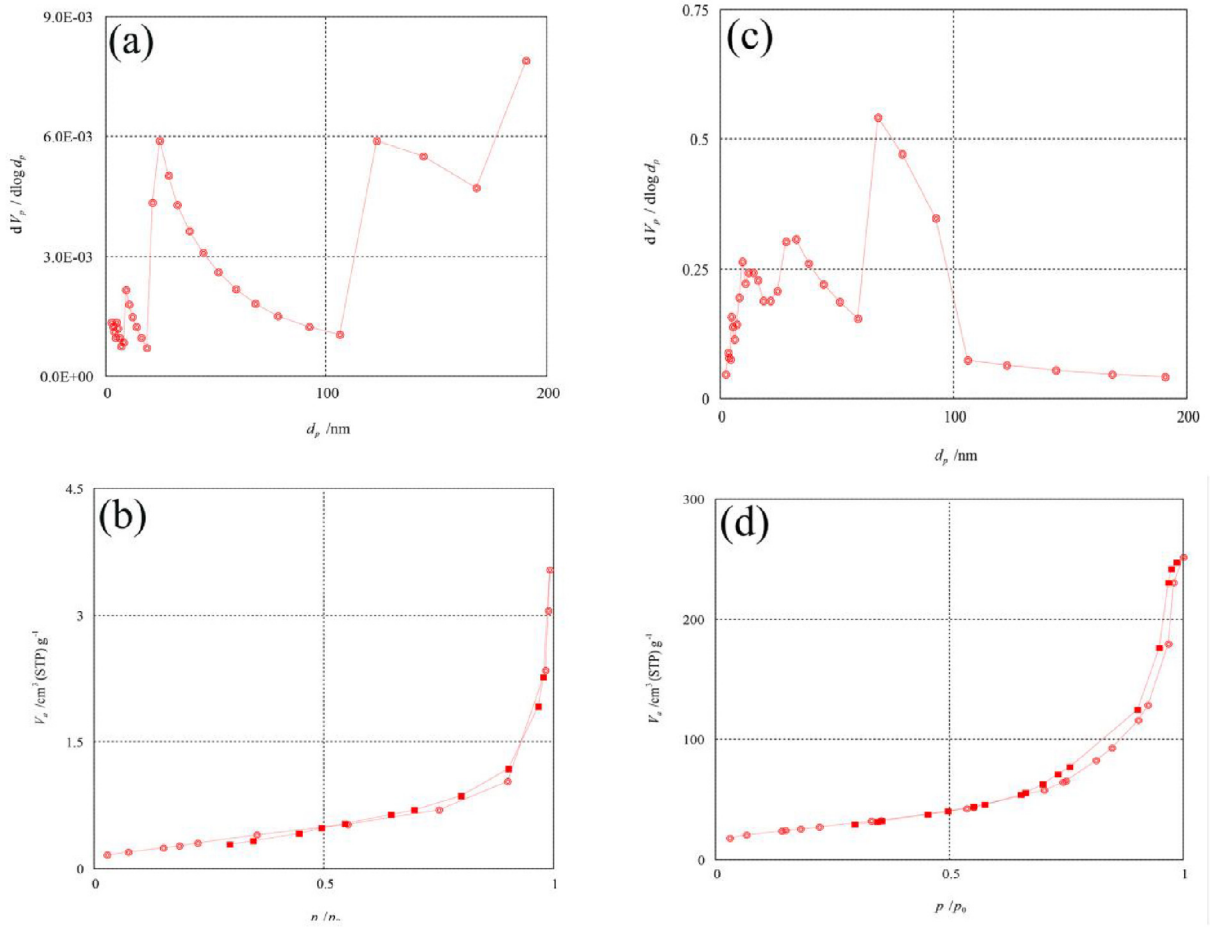

Fig. 9. BET pattern of $ErVO_4/MnWO_4$ heterostructure obtained (a,b) without ultrasonic wave and (c,d) under ultrasonic wave for 20 min with power 180 W.

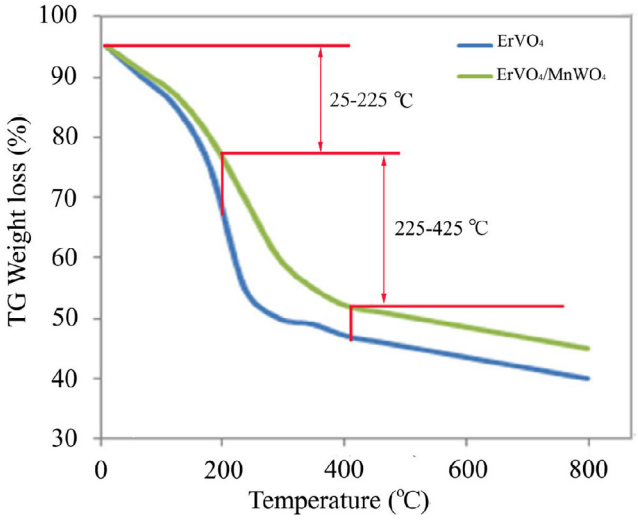

Fig. 10. TGA spectra of (a) $ErVO_4$ and (b) $ErVO_4/MnWO_4$ heterostructure.

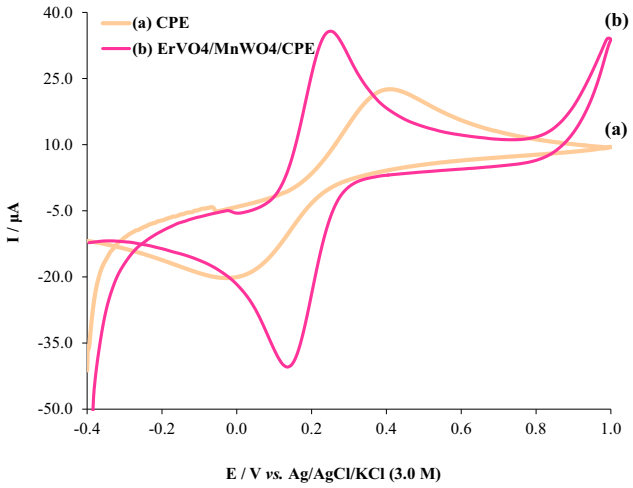

Fig. 11. Cyclic voltammograms of 5.0 mM $[Fe(CN)_6]^{3-/4-}$ in B-R buffer at the surface of (a) CPE and (b) $ErVO_4/MnWO_4$/CPE.

Also for more characterization of the nanostructured modified electrode, EIS technique was used. EIS graphs of the unmodified and modified electrodes in the presence of $[Fe(CN)_6]^{3-/4-}$ (Fe^{2+}/Fe^{3+}) as redox probe is presented in Fig. 12. Significant difference of R_{ct} was observed upon the stepwise formation of the $ErVO_4/MnWO_4$/CPE. The Rc_t values for the bare CPE and $ErVO_4/MnWO_4$/CPE were 5595 Ω cm^2 and 1680 Ω, respectively. The phenomenon can be attributed to the presence of the $ErVO_4/MnWO_4$ heterostructure on the structure of the CPE that accelerates the transfer of the electrons at the surface of the electrode.

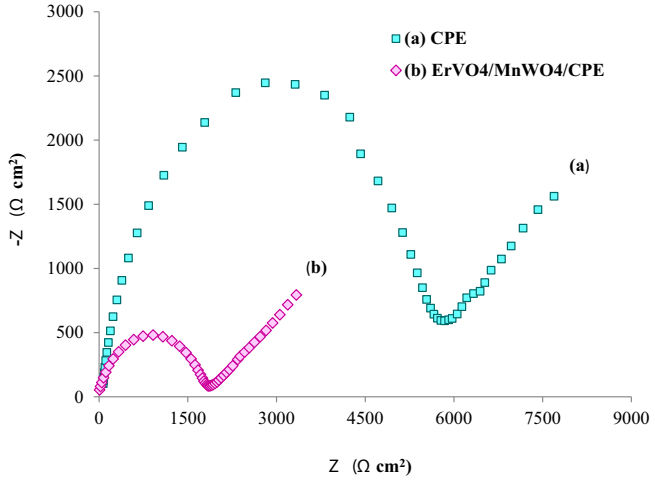

Fig. 12. The Nyquist plots of the bare CPE (a) and modified $ErVO_4/MnWO_4$/CPE (b) the presence of 5.0 mM $[Fe(CN)_6]^{3-/4-}$.

3.5.2. Multivariate optimization by RCCD and RSM

In order to achieve the best results in determination of Tyr, the influences of the different variables were studied using multivariate optimization. In this study, the RCCD method was applied for optimization of chemical and instrumental factors which lead to the higher sensitivity for Tyr amino acid. Therefore, 27 experiments were designed and performed according to the design matrix with coded levels of variables as shown in Table 3. Residuals have been defined as difference between the predicted and the experimental responses and plots of the residuals were applied for sufficiency of the models. Fig. 13 displays that the normal probability plot follows a right line and the residuals randomly disperse in the residual plots. Also, Figs. 14 and 15 show the surface and contour plots of Tyr using DPV responses achieved from the 27 experiments, respectively. Fitness of quadratic model is estimated by the analysis of variance (ANOVA). According to the results obtained from ANOVA and the plots, the optimized values of parameters were calculated and presented in Table 4. Also, the predicted values match the observed values reasonably well with R^2 of 99.71% and adjusted R^2 of 98.37% for response Y. From the data, it can be established that the response equation can generate a suitable and reasonable model for RCCD.

3.5.3. Electrochemical behavior of Tyr at the $ErVO_4/MnWO_4$/CPE

The cyclic voltammogram of Tyr at the surface of bare CPE and modified $ErVO_4/MnWO_4$/CPE were recorded. Fig. 16 displays the voltammograms of B-R buffer solution (pH 7.00) at the surface of a CPE and $ErVO_4/MnWO_4$/CPE in the absence (curve a) and presence of Tyr (curves b, c). The analyte shows a relatively broad and weak oxidation peak at 800 mV (curve b). However, with the $ErVO_4/MnWO_4$/CPE (curve c), the oxidation peak becomes well-defined and sharp, with a magnification of 3.9 times greater than bare CPE and a negative potential shift of 110.0 mV. The lower overpotential and the rise in current response are clear evidence

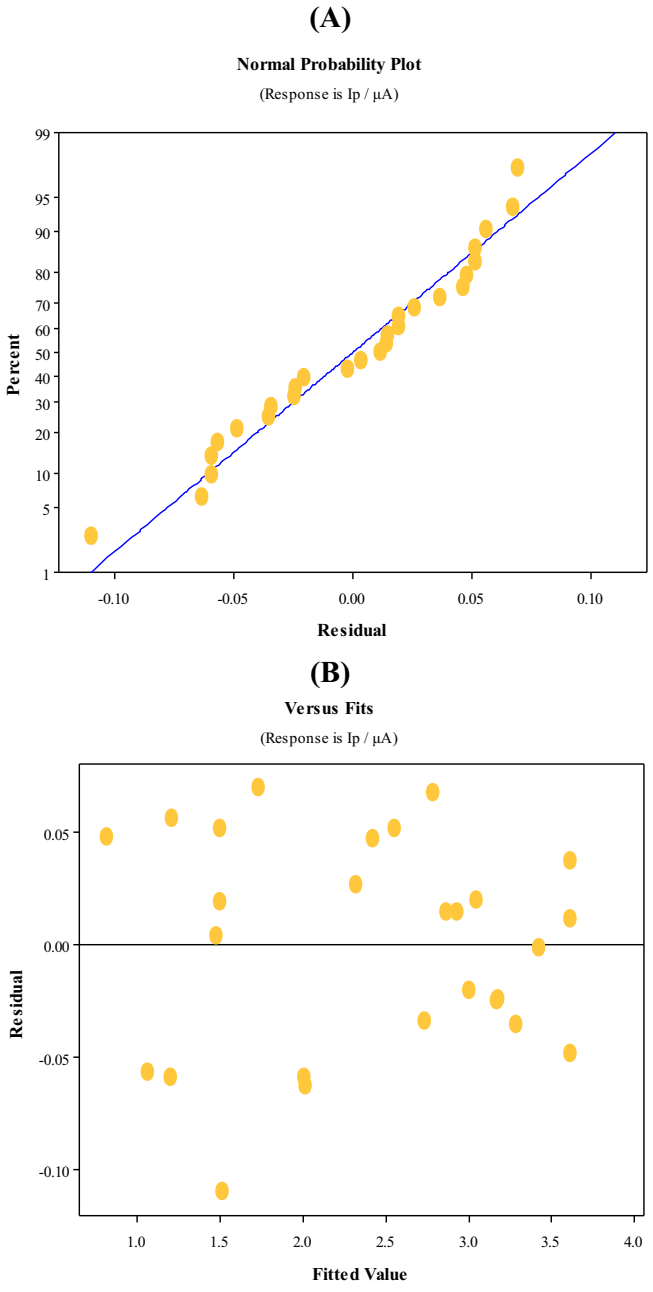

Fig. 13. (A) Residual and (B) normal probability plots of Tyr.

of the electrocatalytic effect of the nanostructured modified electrode on the oxidation of Tyr amino acid.

3.5.4. Determination of Tyr at the $ErVO_4/MnWO_4$/CPE

One of the main purposes of the study is constructing a nanostructured sensitive surface for electrocatalytic determination of

Table 3
Selected coded and actual levels of factors for Tyr.

	Parameters	Coded levels				
	Name	$-\alpha$ (−2)	−1	0	+1	$+\alpha$ (+2)
X_1	*pH*	5.00	6.00	7.00	8.00	9.00
X_2	*$ErVO_4/MnWO_4$ amount (mg)*	1.00	2.00	3.00	4.00	5.00
X_3	*Step potential (V)*	0.001	0.003	0.005	0.007	0.009
X_4	*Pulse height (V)*	0.02	0.03	0.04	0.05	0.06

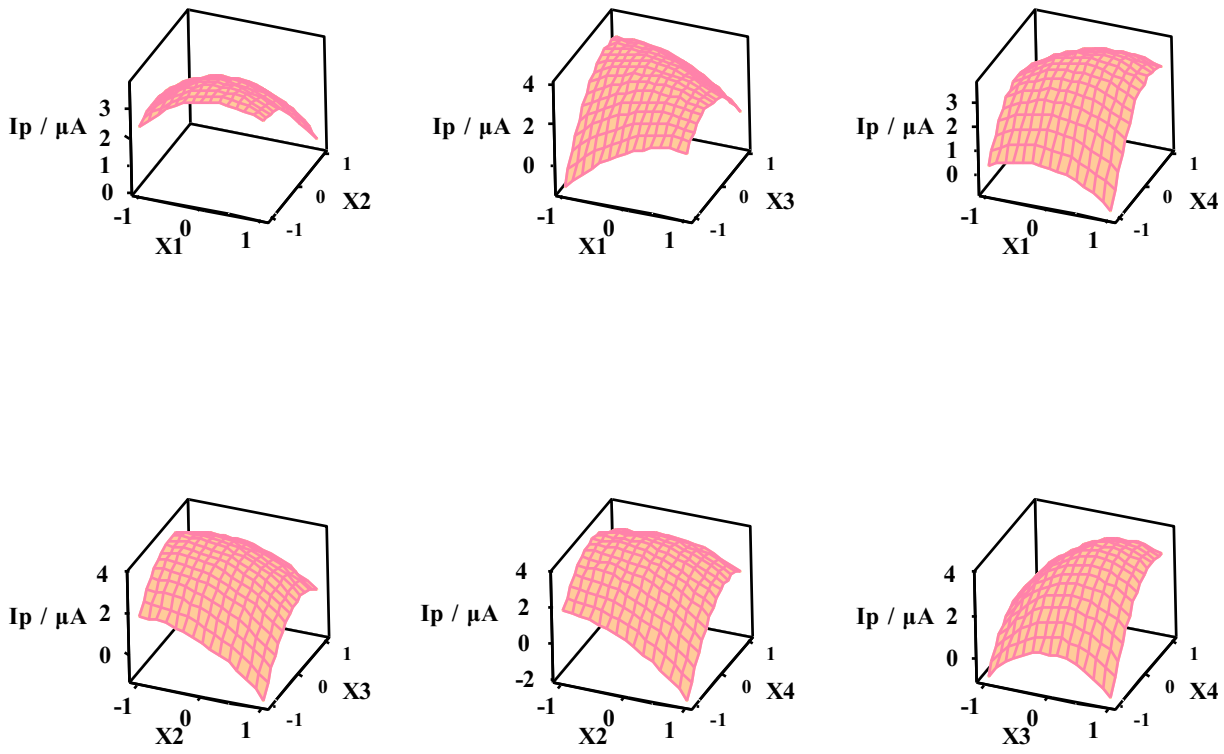

Fig. 14. Surface plots of the interaction effects of pH (X_1), $ErVO_4/MnWO_4$ heterostructure amount (mg, X_2), step potential (V, X_3) and pulse height (V, X_4) on DPV response of Tyr.

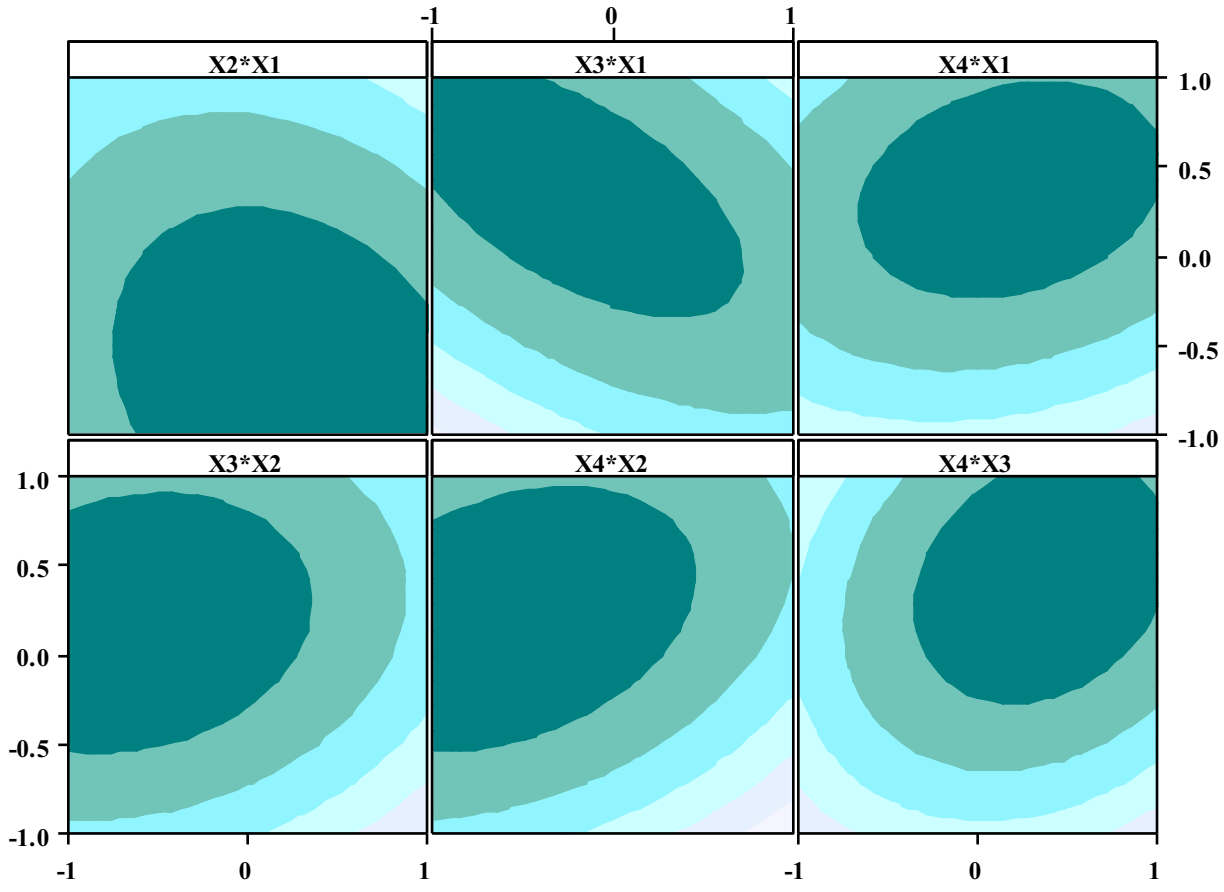

Fig. 15. Contour plots of the interaction effects of pH (X_1), $ErVO_4/MnWO_4$ heterostructure (mg, X_2), step potential (V, X_3) and pulse height (V, X_4) on DPV response of Tyr.

Table 4
Optimized levels of effective parameters on DPV responses of Tyr.

Variables	Optimum values
pH	7.38
$ErVO_4/MnWO_4$ amount (mg)	2.58
Step potential (V)	0.006
Pulse height (V)	0.04

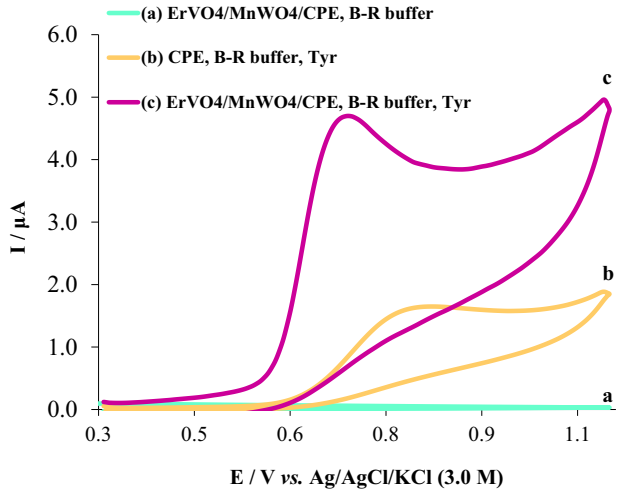

Fig. 16. (a) Cyclic voltammograms of B-R buffer, (a): at $ErVO_4/MnWO_4$/CPE, (b) and (c) in the presence of Tyr at CPE and $ErVO_4/MnWO_4$/CPE, respectively.

Tyr. Therefore, DPV method was applied for estimate of the detection limit of Tyr. Fig. 17(A) shows the differential pulse voltammograms of Tyr in different concentrations at the surface of $ErVO_4/MnWO_4$/CPE under the optimized conditions. Besides, Fig. 17(B) displays the oxidation peak current of Tyr has two linear calibration ranges of 0.08–2.0 µM and 2.0–400.0 µM. According to the

Table 5
Comparison of Tyr determination with different electrochemical sensors.

Sensor	Linear range (µM)	Detection limit (µM)	Reference
Nafion/TiO_2-GR/GCE[a]	10.0–160.0	2.3	[45]
Butyrylcholine/GCE	4.0–100.0	0.4	[46]
ERGO/GCE[b]	0.5–80.0	0.2	[47]
CuO-NPs/CCE[c]	2.0–70.0	0.16	[48]
UT-g-C_3N_4/Ag/GCE[d]	1.0–150.0	0.14	[49]
Ag/Rutin-WGE[e]	0.3–10	0.07	[50]
$ErVO_4/MnWO_4$/CPE	0.08–400.0	0.0077	This work

[a] Nafion/TiO_2-graphene/glassy carbon electrode.
[b] Electrochemically reduced graphene oxide/glassy carbon electrode.
[c] Ccopper oxide nanoparticles/carbon ceramic electrode.
[d] Ultrathin-g-C_3N_4/Ag/glassy carbon electrode.
[e] Silver nanoparticles and Rutin complex film modified paraffin-impregnated graphite electrode.

data, the limit of detection (3σ) of Tyr was obtained 7.7 nM. In Table 5, some of the analytical parameters of the present work are compared with those previously reported by others [40–44]. These data establish that the responses of the proposed sensor are superior to the previously reported literatures.

3.5.5. Interference studies

The influence of common interfering species was studied in the presence of 20.00 µM Tyr using DPV techniques. The results indicated that the concentrations of Na^+, K^+, NH_4^+, Cl^-, CO_3^{2-}, ascorbic acid, acetaminophen, glycine, alanine, phenylalanine, arginine and proline did not significantly influence the height of the oxidation peak current of Tyr at the surface of ErVO4/MnWO4/CPE. The results are listed in Fig. 18. The tolerance limit was considered as the concentrations which give an error of <5.0% in the determination of Tyr.

3.5.6. Real sample analysis

In order to examine the applicability of the proposed method in analysis of real complicated samples, the $ErVO_4/MnWO_4$/CPE was

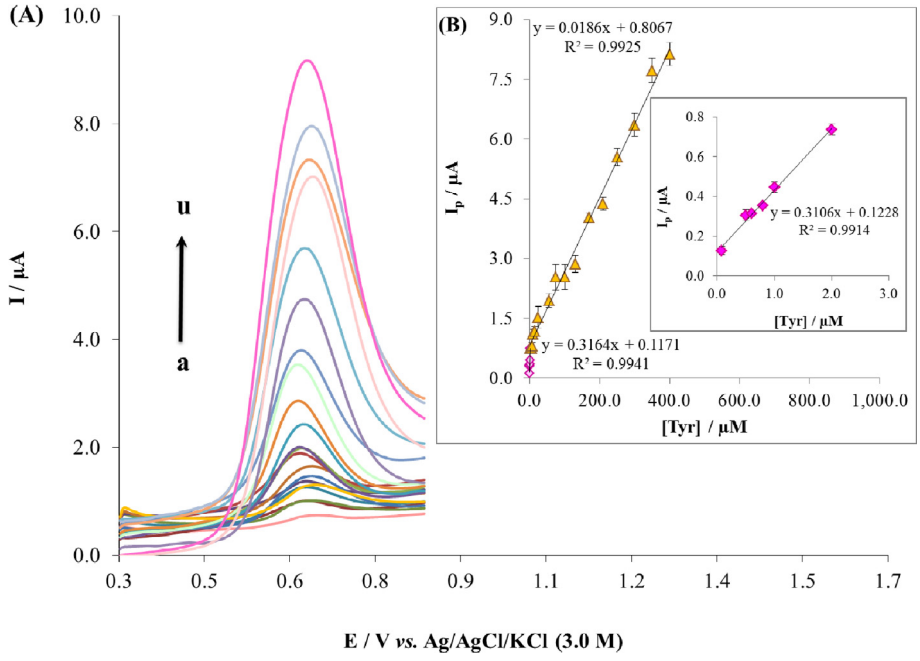

Fig. 17. (A) Differential pulse voltammograms of $ErVO_4/MnWO_4$/CPE in B-R buffer, containing different concentrations of Tyr, a-u correspond to: 0.08–400.0µ M of Tyr and (B) Plot of the peak current as a function of Tyr concentration.

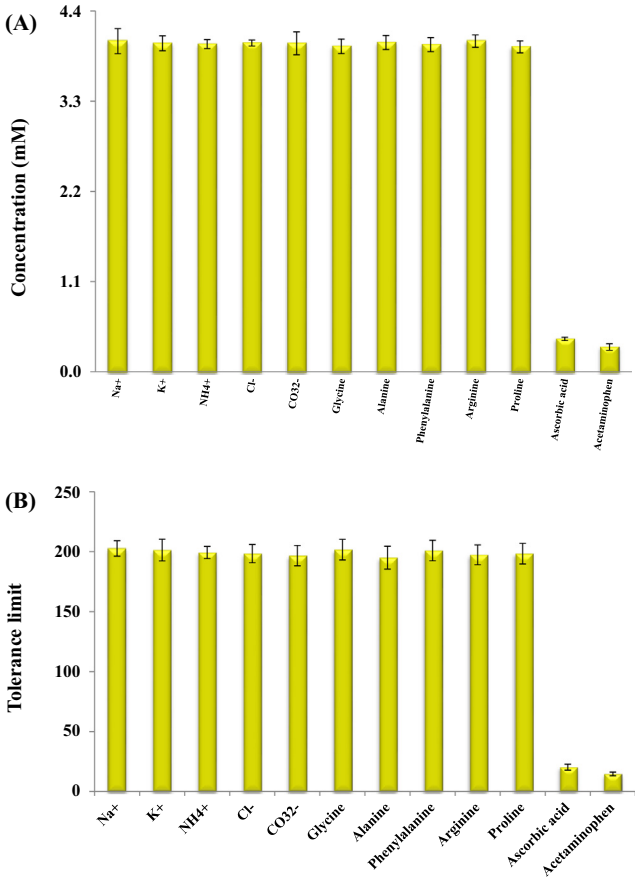

Fig. 18. Plots of (A) concentration and (B) tolerance limit for influence of some foreign substances for Tyr.

Table 6
Determination of Tyr in biological samples at the surface of $ErVO_4/MnWO_4$/CPE.

Sample (*Human blood serum*)	Added (μM)	Found (μM)	Recovery (%)
1	0.0	Not detected	–
2	4.0	3.8	95.0
3	8.0	8.2	102.5
4	12.0	12.4	104.1
5	16.0	15.6	97.5
6	20.0	19.2	96.0

applied for detection of Tyr in human blood serum samples. After analysis by DPV, no Tyr was detected, and as a result spike method was performed. As shown in Table 6, the recovery of 95.0–104.1% was achieved that suggests the nanostructured sensor can be applied successfully to analysis of Tyr in biological samples.

4. Conclusion

This paper reports synthesis of $ErVO_4/MnWO_4$ heterostructure by ultrasonic method with decreased size. The TG indicated that nanostructures have high stability and combining of $MnWO_4$ with $ErVO_4$ ends in increase stability of heterostructures. Additionally, $ErVO_4/MnWO_4$ heterostructure was used for preparation of a nanostructured modified sensor. CV and EIS analysis showed that the nanostructured modified electrode create an excellent electrocatalytic effect for Tyr. A multivariate strategy was used for simultaneous optimization of all effective parameters on the determination of Tyr. Also, the nanostructured sensor has been successfully used for detection of Tyr amino acid in biological complicated samples.

Acknowledgments

Authors are grateful to council of Kashan University of Medical Sciences for providing financial support to undertake this work. This work was supported by Council of Kashan University of Medical Sciences, Kashan, Iran by Grant Agreement No. 97201.

References

[1] H.J. Kim, S.H. Youn, C.S. Shin, Solubility-dependent melting temperature depression of binary substrate mixtures: a model study, Chem. Eng. J. 146 (3) (2009) 449–455.
[2] T. Huang et al., Depression accelerates the development of gastric cancer through reactive oxygen species-activated ABL1, Oncol. Rep. 36 (5) (2016) 2435–2443.
[3] J. Tashkhourian, M. Daneshi, S. Nami-Ana, Simultaneous determination of tyrosine and tryptophan by mesoporous silica nanoparticles modified carbon paste electrode using H-point standard addition method, Anal. Chim. Acta 902 (2016) 89–96.
[4] M. Attia, A.A. Yakout, Novel method for tyrosine assessment in vitro using luminescence quenching of the nano optical sensor Eu–ciprofloxacin doped in a sol–gel matrix, RSC Adv. 6 (25) (2016) 20467–20474.
[5] Q. Sheng et al., Ultrasensitive electrochemical cocaine biosensor based on reversible DNA nanostructure, Biosens. Bioelectron. 51 (2014) 191–194.
[6] L. García-Carmona et al., Filtered carbon nanotubes-based electrodes for rapid sensing and monitoring of L-tyrosine in plasma and whole blood samples, Sens. Actuators, B 259 (2018) 762–767.
[7] G. Neurauter et al., Simultaneous measurement of phenylalanine and tyrosine by high performance liquid chromatography (HPLC) with fluorescence detection, Clin. Biochem. 46 (18) (2013) 1848–1851.
[8] G.D. Pierini et al., Development of an electroanalytical method to control quality in fish samples based on an edge plane pyrolytic graphite electrode. Simultaneous determination of hypoxanthine, xanthine and uric acid, Microchem. J. 138 (2018) 58–64.
[9] Z. Huang, L. Zhang, W. Pan, Synthesis, lattice dynamics, and mechanical properties of a high-pressure scheelite phase of RVO4, Inorg. Chem. 51 (21) (2012) 11235–11237.
[10] S.M. Hosseinpour-Mashkani, A. Sobhani-Nasab, A simple sonochemical synthesis and characterization of CdWO 4 nanoparticles and its photocatalytic application, J. Mater. Sci.: Mater. Electron. 27 (4) (2016) 3240–3244.
[11] A. Sobhani-Nasab et al., Synthesis and characterization of MnWO4/TmVO4 ternary nano-hybrids by an ultrasonic method for enhanced photocatalytic activity in the degradation of organic dyes, Mater. Lett. 238 (2019) 159–162.
[12] S.S. Hosseinpour-Mashkani, A. Sobhani-Nasab, Investigation the effect of temperature and polymeric capping agents on the size and photocatalytic properties of NdVO 4 nanoparticles, J. Mater. Sci.: Mater. Electron. 28 (21) (2017) 16459–16466.
[13] F. Sedighi et al., Synthesis and characterization of CuWO4 nanoparticle and CuWO4/NiO nanocomposite using co-precipitation method; application in photodegradation of organic dye in water, J. Mater. Sci.: Mater. Electron. 29 (16) (2018) 13737–13745.
[14] S.M. Hosseinpour-Mashkani, M. Maddahfar, A. Sobhani-Nasab, Precipitation synthesis, characterization, morphological control, and photocatalyst application of ZnWO 4 nanoparticles, J. Electron. Mater. 45 (7) (2016) 3612–3620.
[15] J.J. Hinman, K.S. Suslick, Nanostructured materials synthesis using ultrasound, in: Sonochemistry, Springer, 2017, pp. 59–94.
[16] A. Sobhani-Nasab et al., Synergetic effect of graphene oxide and C3N4 as co-catalyst for enhanced photocatalytic performance of dyes on Yb2(MoO4)3/YbMoO4 nanocomposite, Ceram. Int. 45 (14) (2019) 17847–17858.
[17] M. Rahimi-Nasrabadi et al., Preparation of Co2TiO4/CoTiO3/polyaniline ternary nano-hybrids for enhanced destruction of agriculture poison and organic dyes under visible-light irradiation, J. Mater. Sci. Mater. Electron. 30 (17) (2019) 15854–15868, https://doi.org/10.1007/s10854-019-01908-7.
[18] S.M. Peymani-Motlagh et al., Assessing the magnetic, cytotoxic and photocatalytic influence of incorporating Yb 3+ or Pr 3+ ions in cobalt–nickel ferrite, J. Mater. Sci.: Mater. Electron. 30 (7) (2019) 6902–6909.
[19] A. Sobhani-Nasab et al., New method for synthesis of BaFe12O19/Sm2Ti2O7 and BaFe12O19/Sm2Ti2O7/Ag nano-hybrid and investigation of optical and photocatalytic properties, J. Mater. Sci.: Mater. Electron. 30 (6) (2019) 5854–5865.
[20] H. Kooshki et al., Eco-friendly synthesis of PbTiO3 nanoparticles and PbTiO3/carbon quantum dots binary nano-hybrids for enhanced photocatalytic performance under visible light, Sep. Purif. Technol. 211 (2019) 873–881.
[21] S.M. Asgarian et al., Investigation of positron annihilation lifetime and magnetic properties of Co1−xCuxFe2O4 nanoparticles, Mater. Res. Express 6 (1) (2018) 015023.
[22] A. Abedini, Nanocrystalline ErVO 4: synthesis, characterization, optical and photocatalytic properties, J. Mater. Sci.: Mater. Electron. 28 (12) (2017) 8446–8451.
[23] Y. Wang et al., Shape-controlled synthesis of MnWO4 nanocrystals by a surfactant-free hydrothermal method, Ceram. Int. 40 (3) (2014) 5085–5090.

[24] M. Eghbali-Arani et al., Green synthesis and characterization of SmVO 4 nanoparticles in the presence of carbohydrates as capping agents with investigation of visible-light photocatalytic properties, J. Electron. Mater. (2018) 1–13.
[25] S. Pourmasoud et al., Investigation of optical properties and the photocatalytic activity of synthesized YbYO4 nanoparticles and YbVO4/NiWO4 nanocomposites by polymeric capping agents, J. Mol. Struct. 1157 (2018) 607–615.
[26] A. Sobhani-Nasab et al., Preparation, characterization and investigation of sonophotocatalytic activity of thulium titanate/polyaniline nanocomposites in degradation of dyes, Ultrason. Sonochem. 50 (2019) 46–58.
[27] S.M. Hosseinpour-Mashkani, A. Sobhani-Nasab, M. Mehrzad, Controlling the synthesis SrMoO4 nanostructures and investigation its photocatalyst application, J. Mater. Sci.: Mater. Electron. 27 (6) (2016) 5758–5763.
[28] S. Luo et al., Rational and green synthesis of novel two-dimensional WS2/MoS2 heterojunction via direct exfoliation in ethanol-water targeting advanced visible-light-responsive photocatalytic performance, J. Colloid Interface Sci. 513 (2018) 389–399.
[29] S.S. Hosseinpour-Mashkani, S.S. Hosseinpour-Mashkani, A. Sobhani-Nasab, Synthesis and characterization of rod-like CaMoO 4 nanostructure via free surfactant sonochemical route and its photocatalytic application, J. Mater. Sci.: Mater. Electron. 27 (5) (2016) 4351–4355.
[30] S.M. Hosseinpour-Mashkani, M. Maddahfar, A. Sobhani-Nasab, Novel silver-doped CdMoO4: synthesis, characterization, and its photocatalytic performance for methyl orange degradation through the sonochemical method, J. Mater. Sci.: Mater. Electron. 27 (1) (2016) 474–480.
[31] M.A. Marsooli et al., Preparation and characterization of magnetic Fe3O4/CdWO4 and Fe3O4/CdWO4/PrVO4 nanoparticles and investigation of their photocatalytic and anticancer properties on PANC1 cells, Materials 12 (19) (2019) 3274.
[32] H. Eskandarloo et al., Ultrasonic-assisted degradation of phenazopyridine with a combination of Sm-doped ZnO nanoparticles and inorganic oxidants, Ultrason. Sonochem. 28 (2016) 169–177.
[33] G. Gyawali et al., Sonochemical synthesis of solar-light-driven Ag-PbMoO4 photocatalyst, J. Hazard. Mater. 263 (2013) 45–51.
[34] R. Monsef, M. Ghiyasiyan-Arani, M. Salavati-Niasari, Application of ultrasound-aided method for the synthesis of NdVO4 nano-photocatalyst and investigation of eliminate dye in contaminant water, Ultrason. Sonochem. 42 (2018) 201–211.
[35] M. Eghbali-Arani et al., Ultrasound-assisted synthesis of YbVO4 nanostructure and YbVO4/CuWO4 nanocomposites for enhanced photocatalytic degradation of organic dyes under visible light, Ultrason. Sonochem. 43 (2018) 120–135.
[36] R.V. Kumar, Y. Diamant, A. Gedanken, Sonochemical synthesis and characterization of nanometer-size transition metal oxides from metal acetates, Chem. Mater. 12 (8) (2000) 2301–2305.
[37] A. Rodríguez-Martínez et al., Characterization of nanoparticles doped composites using ultrasound, Ultrasonics 83 (2018) 68–79.
[38] A. Sobhani-Nasab et al., Sonochemical synthesis of terbium tungstate for developing high power supercapacitors with enhanced energy densities, Ultrason. Sonochem. 45 (2018) 189–196.
[39] A. Karthika et al., Electrochemical sensing of nicotine using CuWO4 decorated reduced graphene oxide immobilized glassy carbon electrode, Ultrason. Sonochem. (2019).
[40] Y. Fan et al., Electrochemistry and voltammetric determination of L-tryptophan and L-tyrosine using a glassy carbon electrode modified with a Nafion/TiO2-graphene composite film, Microchim. Acta 173 (1–2) (2011) 241–247.
[41] G.-P. Jin, X.-Q. Lin, The electrochemical behavior and amperometric determination of tyrosine and tryptophan at a glassy carbon electrode modified with butyrylcholine, Electrochem. Commun. 6 (5) (2004) 454–460.
[42] K.-Q. Deng, J.-H. Zhou, X.-F. Li, Direct electrochemical reduction of graphene oxide and its application to determination of L-tryptophan and L-tyrosine, Colloids Surf., B 101 (2013) 183–188.
[43] H. Razmi, H. Nasiri, R. Mohammad-Rezaei, Amperometric determination of L-tyrosine by an enzymeless sensor based on a carbon ceramic electrode modified with copper oxide nanoparticles, Microchim. Acta 173 (1–2) (2011) 59–64.
[44] A. Khoshroo et al., Development of electrochemical sensor for sensitive determination of oxazepam based on silver-platinum core–shell nanoparticles supported on graphene, J. Electroanal. Chem. 823 (2018) 61–66.
[45] Y. Fan, J. Liu, H. Lu, Q. Zhang, Electrochemistry and voltammetric determination of L-tryptophan and L-tyrosine using a glassy carbon electrode modified with a Nafion/TiO2-graphene composite film, Microchim. Acta 173 (2011) 241–247.
[46] G. Jin, X. Lin, The electrochemical behavior and amperometric determination of tyrosine and tryptophan at a glassy carbon electrode modified with butyrylcholine, Electrochem. Comm. 6 (2004) 454–460.
[47] K. Deng, J. Zhou, X. Li, Direct electrochemical reduction of graphene oxide and its application to determination of L-tryptophan and L-tyrosine, Colloid. Surf. B 101 (2013) 183–188.
[48] H. Razmi, H. Nasiri, R. Mohammad-Rezaei, Amperometric determination of L-tyr-osine by an enzymeless sensor based on a carbon ceramic electrode modified with copper oxide nanoparticles, Microchim. Acta 173 (2011) 59–64.
[49] J. Zou, D. Mao, A.T.S. Wee, J. Jiang, Micro/nano-structured ultrathin g-C_3N_4/Ag nanoparticle hybrids as efficient electrochemical biosensors forL-tyrosine, Applied Surface Science 467–468 (2019) 608–618.
[50] G. Jin, X. Peng, Q. Chen, Preparation of novel arrays silver nanoparticles modified polyrutin coat-paraffin-impregnated graphite electrode for tyrosine and tryptophans oxidation, Electroanalysis 20 (2008) 907–915.